Electronic Supplementary Material (ESI) for Organic Chemistry Frontiers.

Supporting Information

for

Effect of Fluorine SubstitutioninOrganoboron Electron Acceptors for Photovoltaic Application

Fangbin Liu, Jun Liu* and Lixiang Wang

State Key Laboratory of Polymer Physics and Chemistry, Changchun Institute of Applied Chemistry, Chinese Academy of Sciences, Changchun 130022, People's Republic of China.

E-mail: liujun@ciac.ac.cn

Contents

1. PSC device fabrication and measurements

OSC device was fabricated with an architecture of indium tin oxide (ITO)/ poly(3,4-ethylenedioxythiophene) doped with polystyrene sulfonate (PEDOT:PSS)/active layer/Ca/Al. Patterned ITO glass substrates were cleaned by sequential ultrasonication in detergent, deionized water, acetone, and isopropyl alcohol, followed by heating at 120 ^{o}C for 30 min and treating with UV-ozone for 30 min. PEDOT:PSS (Baytron PVP Al4083)was spin-coated on the ITO substrates at a speed of 5000 rpm for 40 s to give a thickness of 40 nm, and then baked at 120 ^{o}C for 30 min. The active layers was spin-coated from the solution of PBDB-T:**MBN**, PBDB-T:**MBN-F1** and PBDB-T:**MBN-F2** with a donor:acceptor ratio of 1:1 (*w*/*w*) in chlorobenzene (20 mg mL^{-1}). The active layer was annealed at 100 ^{o}Cfor10 minutes in N_2 atmosphere. Finally, the device was transferred to a vacuum chamber, and Ca (20 nm)/Al (100 nm) was sequentially deposited by thermal evaporation at the pressure of about 2×10^{-4} Pa. The active area of each device was 8.0 mm^2.

The current density (*J*-*V*) curves of the OSC devices were measured using a computer-controlled Keithley 2400 source meter under 100 mW cm^{-2} AM 1.5G simulated solar light illumination provided by a XES-40S2-CE Class Solar Simulator (Japan, SAN-EIElectric Co., Ltd.).The EQE was measured using a Solar Cell Spectral Response Measurement System QE-R3011 (Enlitech Co., Ltd.), which was calibrated with a crystal silicon photovoltaic cell before use.

2. Thermal property

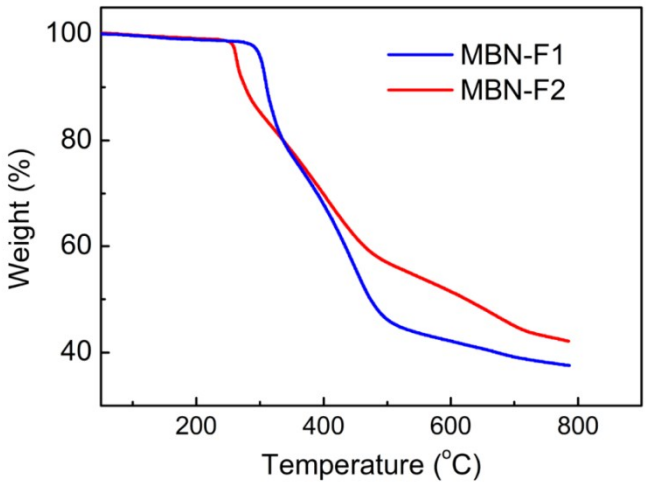

Figure S1. TGA curves of **MBN-F1** and **MBN-F2**.

Thermpgracimetric analysis (TGA) was performed to investigate thermal properties of **MBN-F1** and **MBN-F2** in N_2 flow. As shown in Figure S1, **MBN-F1** and **MBN-F2** exhibit good thermal stability with thermal decomposition temperature (T_d) at 302 and 264 °C for 5% weight loss at heating rate of 20 °C/min.

3. DFT calculation results

All calculations were carried out using Gaussian 09. The geometry structures of MBN-F1, MNB-F2 and two other fluorinated molecules were optimized by using DFT calculations (B3LYP/6-31G(d,p)) and the alkyl chains have been replaced by methyl for clarity. One fluorinated molecule possesses pentafluorophenyl substituent on the organoboron core unit. The other one is an eight-fold fluorinated MBN-derivative (both at the organoboron core unit and at the endcapping groups).

Molecule	Chemical structure	LUMO	HOMO
MBN	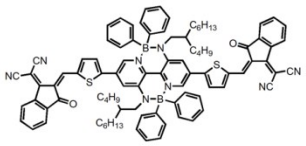	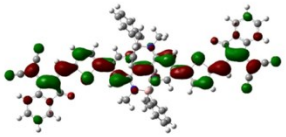	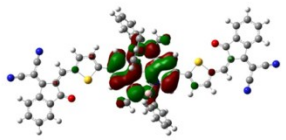
MBN-F1	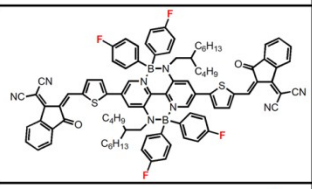	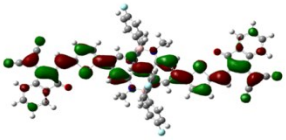	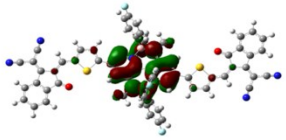
MBN-F2	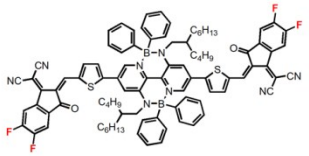	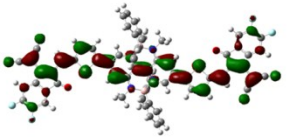	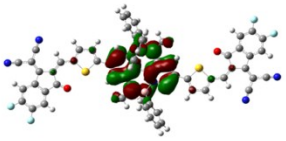
MBN-F3	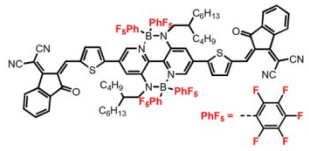	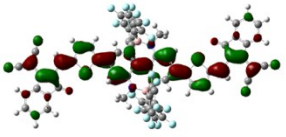	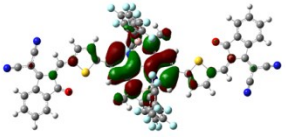
MBN-F4	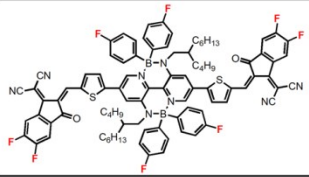	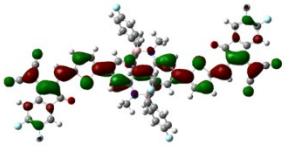	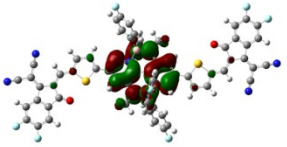

Figure S2. The chemical structures and Kohn–Sham LUMOs and HOMOs of **MBN**, **MBN-F1**, **MBN-F2** and two other fluorinated molecules.

Time-dependent DFT (TD-DFT) calculations were performed at the B3LYP/6-

31G(d) level of theory to elucidate the absorption spectra of MBN-F1 and MNB-F2. The $S_0 \rightarrow S_n$ transitions of TD-DFT calculation were then performed based on the optimized structure at ground state. The TD-DFT calculation results were as follows.

(1) Excitation energies and oscillator strengths of **MBN-F1** (oscillator strength exceeding 0.1)**:**

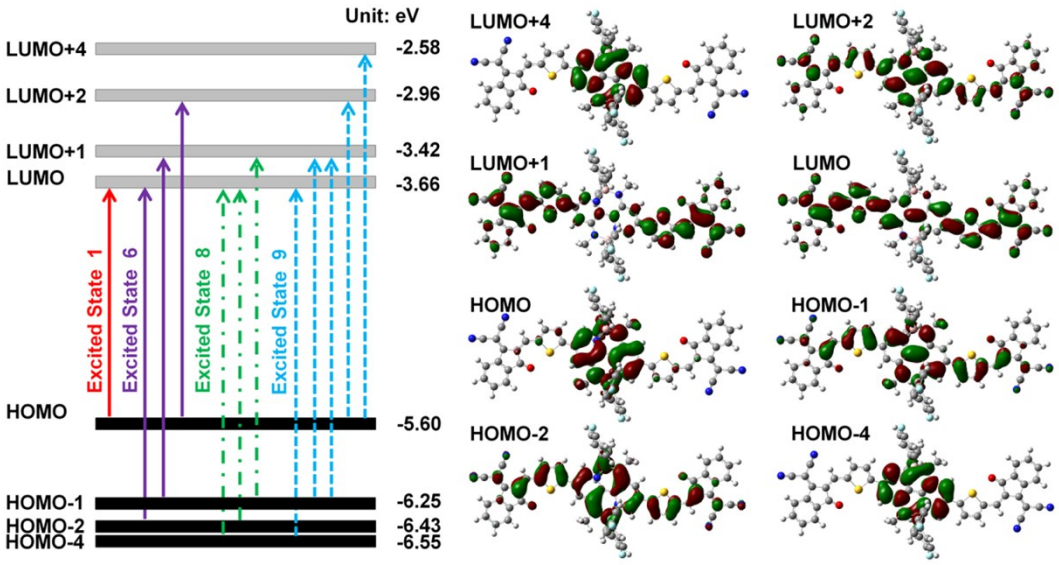

Figure S3. Schematic diagrams showing the main orbital configurations and electronic transitions (oscillator strength exceeding 0.2) of **MBN-F1** based on the TD-DFT calculation.

Excited State 1: Energy: 1.6439 eV Wavelength: 754.23 nm Oscillator strength: 0.5821 Configurations:

HOMO→LUMO 0.70407

Excited State 4: Energy: 2.3327 eV Wavelength: 531.51 nm Oscillator strength: 0.1303 Configurations:

HOMO→LUMO+2 0.68557

HOMO→LUMO+4 -0.12704

Excited State 6: Energy: 2.5220 eV Wavelength: 491.61 nm Oscillator strength: 0.8547 Configurations:

HOMO-2→LUMO -0.36842

HOMO-1→LUMO+1 0.58239

HOMO→LUMO+4 -0.10381

Excited State 8: Energy: 2.5347 eV Wavelength: 489.14 nm Oscillator

strength: 0.2255 Configurations:

HOMO-4→LUMO	0.26853
HOMO-2→LUMO	0.52383
HOMO-1→LUMO+1	0.36807

Excited State 9: Energy: 2.6108 eV Wavelength: 474.88 nm Oscillator strength: 0.2280 Configurations:

HOMO-4→LUMO	-0.45873
HOMO-2→LUMO	0.10677
HOMO-1→LUMO+1	0.12431
HOMO→LUMO+2	0.12056
HOMO→LUMO+4	0.48420

Excited State 10: Energy: 2.6445 eV Wavelength: 468.83 nm Oscillator strength: 0.1228 Configurations:

HOMO-6→LUMO	-0.26625
HOMO-4→LUMO	0.41977
HOMO-2→LUMO	-0.20559
HOMO→LUMO+4	0.43845

Excited State 12: Energy: 2.7189 eV Wavelength: 456.01 nm Oscillator strength: 0.1913 Configurations:

HOMO-6→LUMO	0.64005
HOMO-4→LUMO	0.16082
HOMO-2→LUMO	-0.15182
HOMO→LUMO+4	0.16120

Excited State 25: Energy: 3.1177 eV Wavelength: 397.68 nm Oscillator strength: 0.1877 Configurations:

HOMO-15→LUMO+1	-0.21714
HOMO-15→LUMO+3	-0.15098
HOMO-14→LUMO	0.33947
HOMO-14→LUMO+4	0.10855
HOMO-7→LUMO+1	0.32247
HOMO-5→LUMO+1	-0.18539

HOMO-2→LUMO+2 -0.16728

HOMO-1→LUMO+3 0.33633

The above results indicate that the short-wavelength absorption band of **MBN-F1** is mainly attributed to the HOMO-4→LUMO, HOMO-2→LUMO, HOMO-1→LUMO+1, HOMO→LUMO+2, HOMO→LUMO+4 transitions (illustrated by excited state 6, 8 and 9 in Figure S3). The long-wavelength absorption band of **MBN-1** is mainly attributed to the HOMO→LUMO transition.

(2) Excitation energies and oscillator strengths of **MBN-F2** (oscillator strength exceeding 0.1):

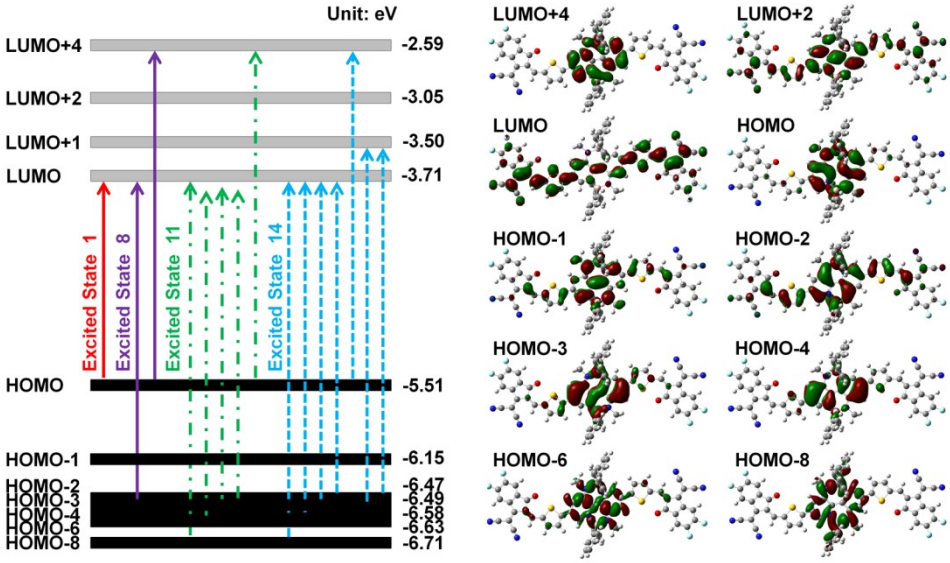

Figure S4. Schematic diagrams showing the main orbital configurations and electronic transitions (oscillator strength exceeding 0.2) of **MBN-F2** based on the TD-DFT calculation.

Excited State 1: Energy: 1.4671 eV Wavelength: 845.12 nm Oscillator strength: 0.4882 Configurations:

HOMO→LUMO 0.70473

Excited State 6: Energy: 2.2732 eV Wavelength: 545.41 nm Oscillator strength: 0.1745 Configurations:

HOMO-1→LUMO+1 0.70079

Excited State 8: Energy: 2.4444 eV Wavelength: 507.22 nm Oscillator strength: 0.6059 Configurations:

HOMO-3→LUMO -0.42627

HOMO→LUMO+4 0.54410

Excited State 11: Energy: 2.5668 eV Wavelength: 483.04 nm Oscillator strength: 0.3235 Configurations:

HOMO-8→LUMO 0.19346

HOMO-6→LUMO 0.36813

HOMO-4→LUMO 0.52451

HOMO-3→LUMO -0.15758

HOMO→LUMO+4 -0.12102

Excited State 12: Energy: 2.5882 eV Wavelength: 479.04 nm Oscillator strength: 0.1864 Configurations:

HOMO-8→LUMO -0.20366

HOMO-6→LUMO 0.58516

HOMO-4→LUMO -0.26361

HOMO-3→LUMO 0.14831

HOMO→LUMO+4 0.11000

Excited State 14: Energy: 2.6558 eV Wavelength: 466.84 nm Oscillator strength: 0.4426 Configurations:

HOMO-8→LUMO 0.62339

HOMO-4→LUMO -0.21257

HOMO-3→LUMO 0.12129

HOMO-2→LUMO 0.12520

HOMO→LUMO+4 0.11556

HOMO-3→LUMO+1 0.64219

HOMO-2→LUMO+1 -0.13744

The above results indicate that the short-wavelength absorption band of **MBN-F2** is mainly attributed to the HOMO-8→LUMO, HOMO-6→LUMO, HOMO-4→LUMO, HOMO-3→LUMO, HOMO-3→LUMO+1, HOMO-2→LUMO, HOMO-1→LUMO+1, HOMO→LUMO+2, HOMO→LUMO+4 transitions (illustrated by excited state 8, 11 and 14 in Figure S4). The long-wavelength absorption band of MBN-1 is mainly attributed to the HOMO→LUMO transition.

4. Charge mobility measurement

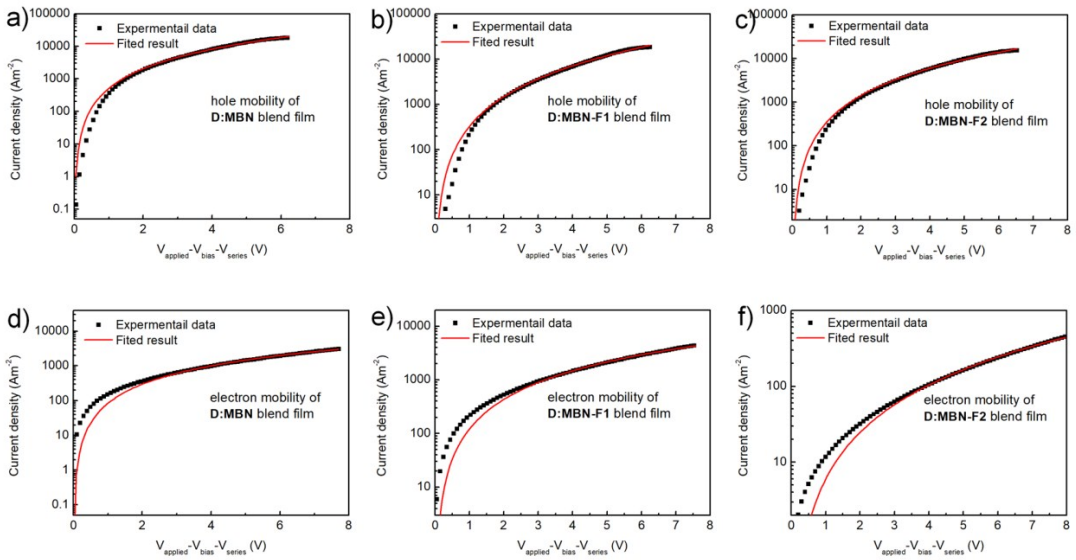

Figure S5. *J-V* curves and SCLC fitting of the hole-only device (a, b and c) and electron-only device (d, e and f) of the blend films based on PBDB-T:**MBN**, PBDB-T:**MBN-F1** and PBDB-T:**MBN-F2**.

Charge mobilities of the blend films based on PBDB-T:**MBN**, PBDB-T:**MBN-F1** and PBDB-T:**MBN-F2** were measured based on the space-charge-limited current (SCLC) method based on the *J-V* curves of the hole-only device (ITO/PEDOT:PSS/active layer/Al) and electron-only device (ITO/PEIE/active layer/Ca/Al). The *J-V* curves in the range of 0-10 V were recorded and fitted to a space-charge-limited function:

$$J = \frac{9\varepsilon_0\varepsilon_r\mu_0 V^2}{8L^3} exp\left(0.89\beta\sqrt{\frac{V}{L}}\right) \quad (1)$$

where J is the current density, L is the film thickness of the active layer, μ_0 is the charge mobility, ε_r is the relative dielectric constant of the transport medium, ε_0 is the permittivity of free space, V (V_{appl} - V_{bi}) is the internal voltage in the device, where V_{appl} is the applied voltage to the device and V_{bi} is the built-in voltage due to the relative work function difference of the two electrodes. β is the field-activation factor.

The hole mobilities of the active layers are 1.11×10^{-4} cm^2 V^{-1} s^{-1} for **MBN**, 1.07×10^{-4} cm^2 V^{-1} s^{-1} for **MBN-F1** and 1.42×10^{-4} cm^2 V^{-1} s^{-1} for **MBN-F2**. The electron mobilities of the active layers are 1.88×10^{-5} cm^2 V^{-1} s^{-1} for **MBN**, 2.71×10^{-5} cm^2 V^{-1} s^{-1} for **MBN-F1** and 2.40×10^{-6} cm^2 V^{-1} s^{-1} for **MBN-F2**.

5. J_{sc} versus light intensity and J_{ph} versus effective voltage

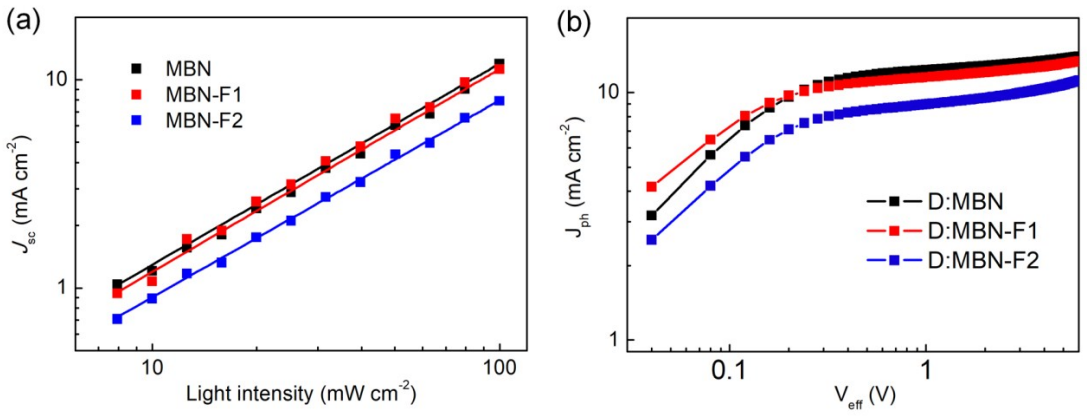

Figure S6. (a) Dependence of J_{sc} on illuminated light intensity dependence and (b) photocurrent versus effective voltage (V_{eff}) for the OSCs based on PBDB-T:**MBN**, PBDB-T:**MBN-F1** and PBDB-T:**MBN-F2**.

To gain more insight into the charge-recombination mechanism and exciton dissociation processes occurring in the device, we investigate the J_{sc} as a function of light intensity (P) and exciton dissociation probabilities, and the corresponding fitting results are shown in Figure S6. The J_{sc} as a function of illuminated light intensity was performed by varing light intensity from 1 to 100 mW cm^{-2}, and the corresponding equation is described as $J_{sc} \propto P^{\alpha}$, where α is the slope of the lines in logarithmic scale. If α is equal to or approximates to 1, it indicates there is the negligible bimolecular recombination in the device at the short circuit condition. As shown in Figure S6a, the values of **MBN**, **MBN-F1**, and **MBN-F2**-based devices were estimated to be 0.967, 0.973 and 0.946. The results suggest that the **MBN-F2**-based device has more bimolecular charge recombination under short-circuit conditions than that of the other two devices. In addition, as shown in Figure S6b, the exciton dissociation probability of PBDB-T:**MBN** based device is 76.4%, which is much higher than that of PBDB-T:**MBN-F1** based device (75.6%) and PBDB-T:**MBN-F2** based device (66.7%). The charge carrier generation/collection efficiency of three devices are relatively low (<80%), indicating possible inefficient exciton dissociation.

6. ^{1}H NMR, ^{13}C NMR and mass spectra

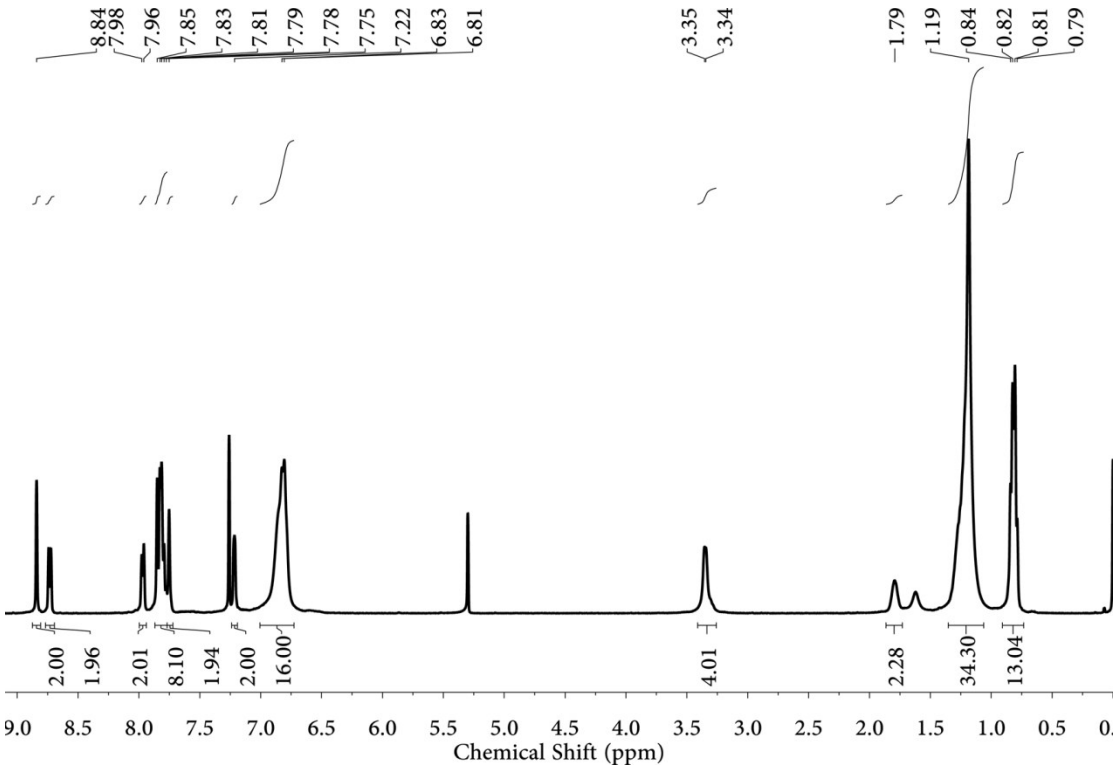

Figure S7. ^{1}H NMR spectrum of **MBN-F1**.

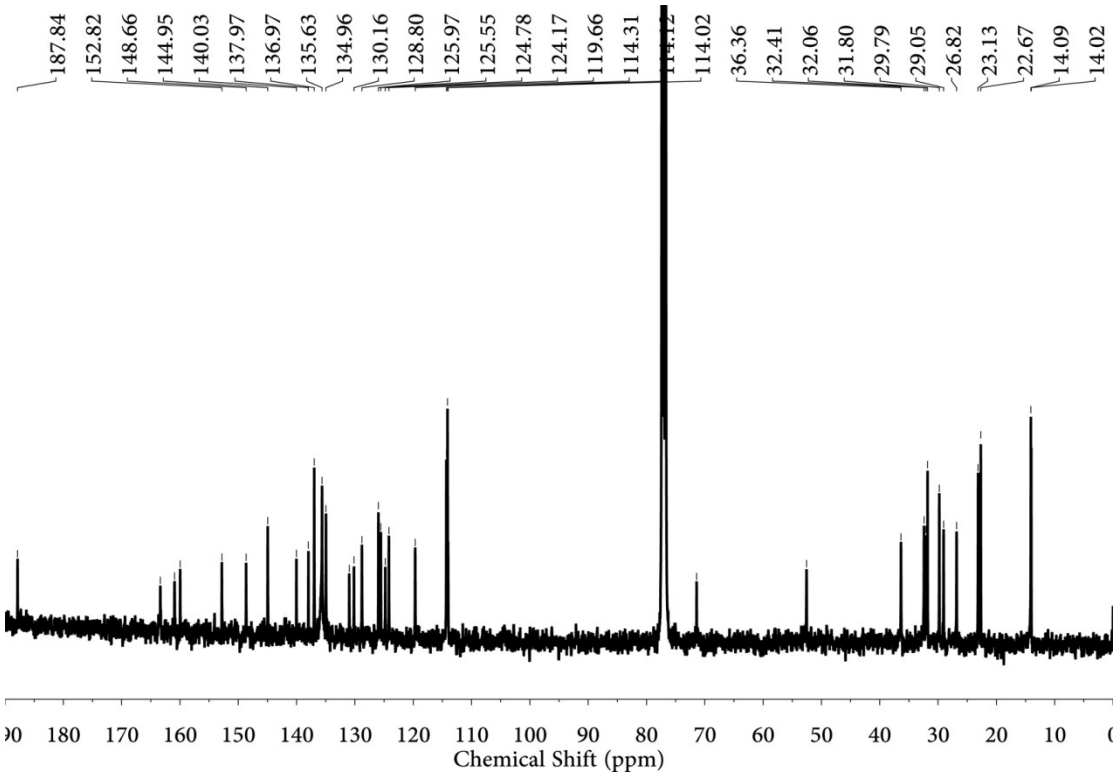

Figure S8. ^{13}C NMR spectrum of **MBN-F1**.

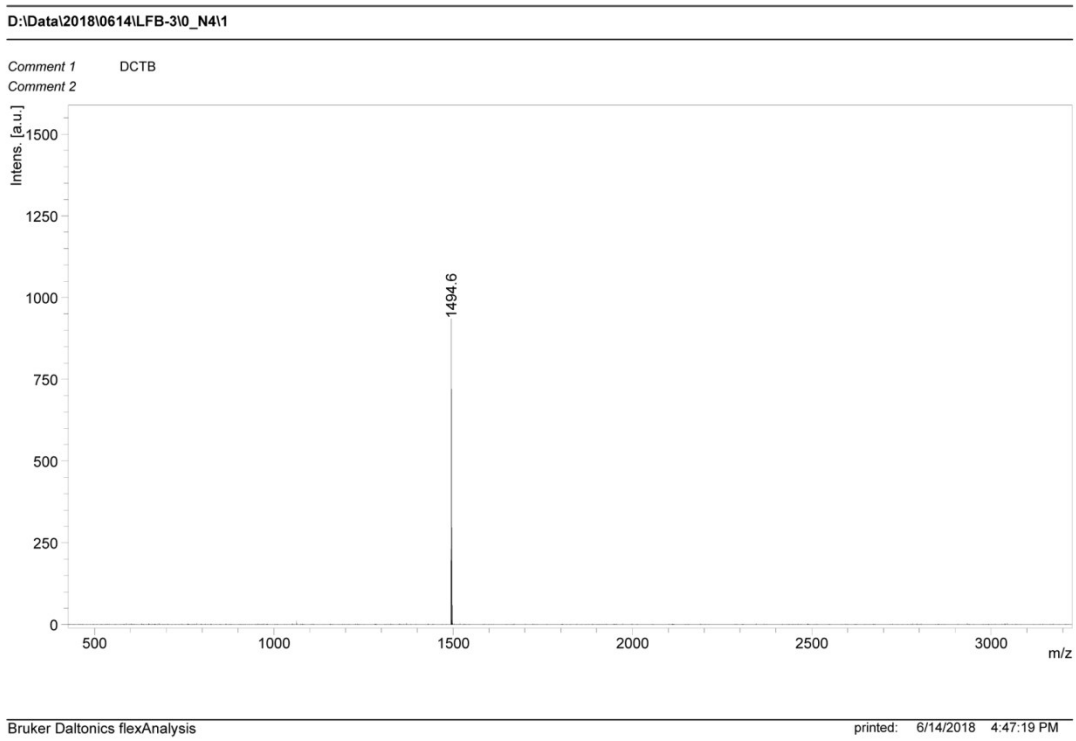

Figure S9. MALDI-TOF mass spectrum of **MBN-F1**.

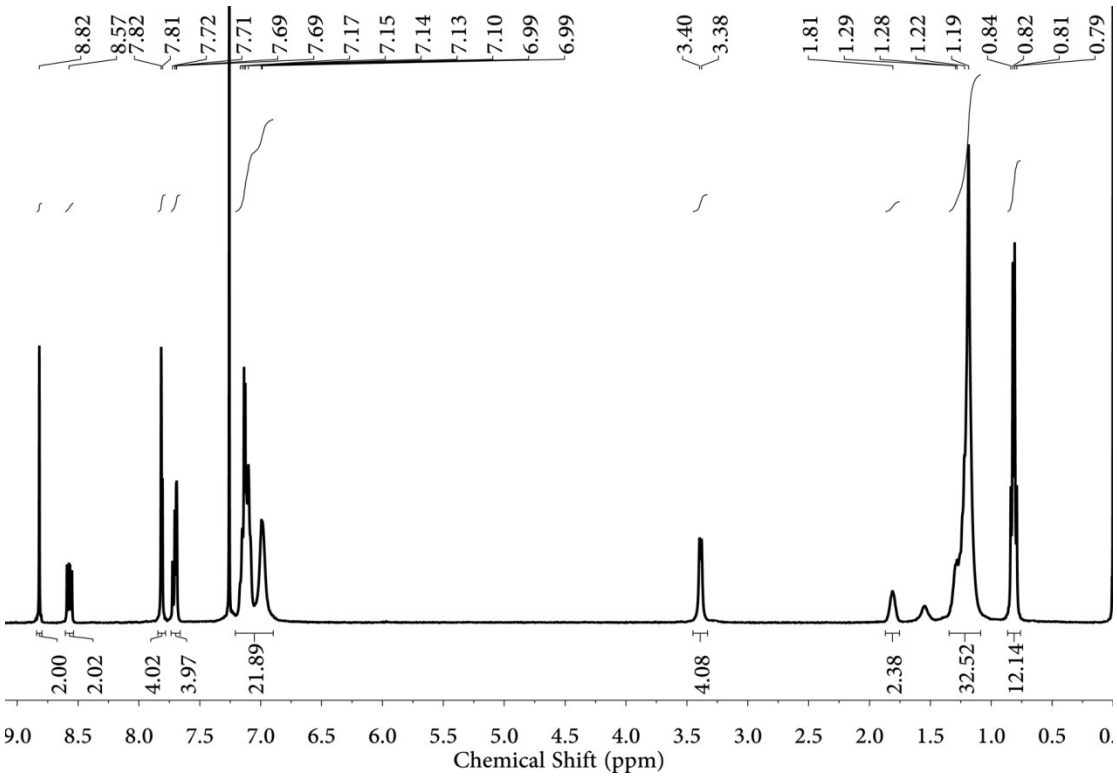

Figure S10. ^{1}H NMR spectrum of **MBN-F2**.

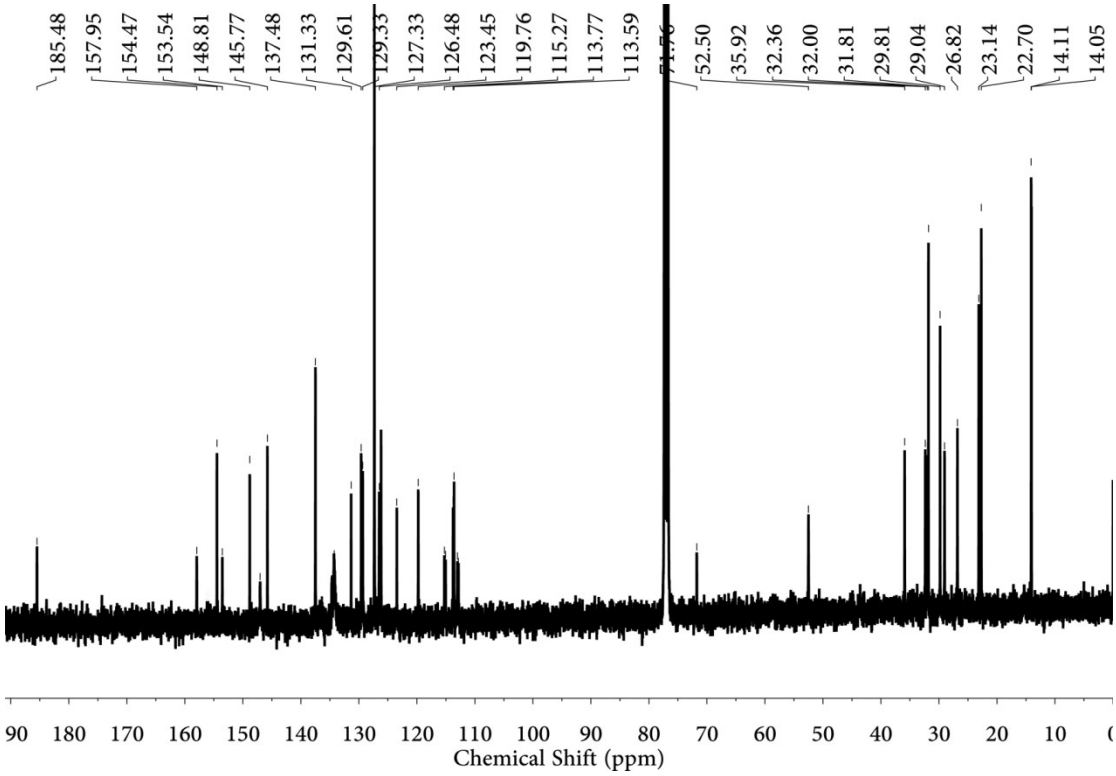

Figure S11. ^{13}C NMR spectrum of **MBN-F2**.

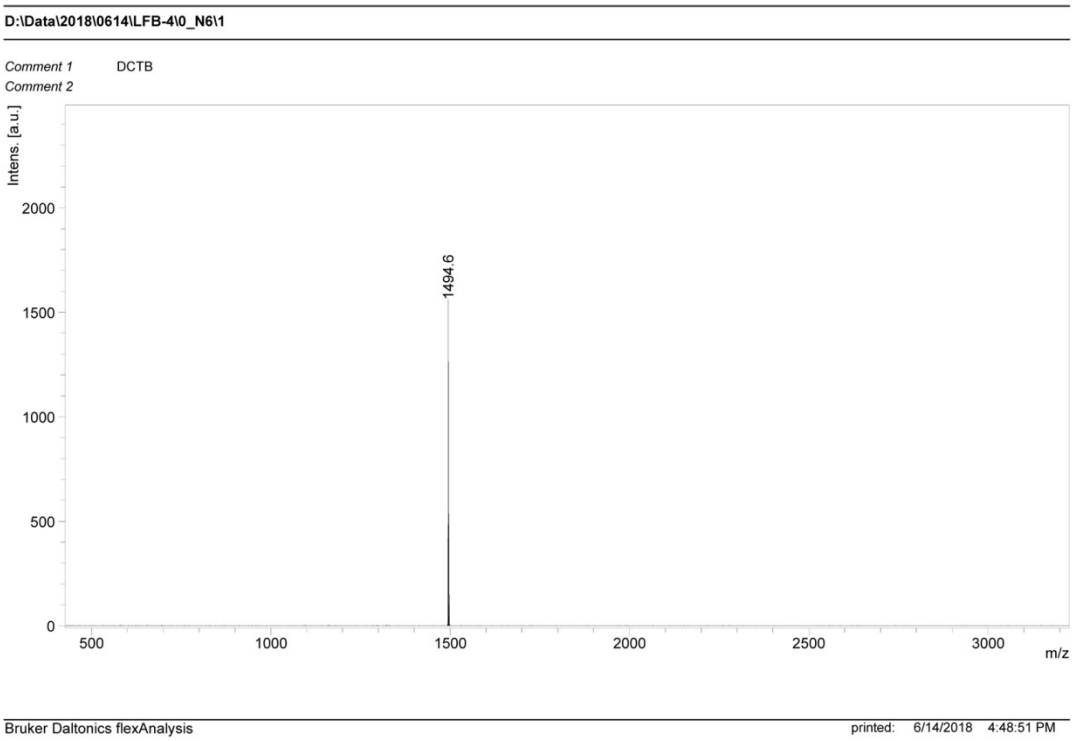

Figure S12. MALDI-TOF mass spectrum of **MBN-F2**.